Absolute total, partial, and differential cross sections for photodetachment of O^-

Matthieu Génévriez,[1,*] Kevin M. Dunseath,[2] Mariko Terao-Dunseath,[2] Alan Hibbert,[3] Arnaud Dochain,[1] Raphaël Marion,[1] and Xavier Urbain[1,†]

[1]*Institute of Condensed Matter and Nanosciences, Université Catholique de Louvain, Louvain-la-Neuve B-1348, Belgium*

[2]*Univ Rennes, CNRS, IPR (Institut de Physique de Rennes)-UMR 6251, F-35000 Rennes, France*

[3]*Department of Applied Mathematics and Theoretical Physics, Queen's University, Belfast BT7 1NN, United Kingdom*

(Received 13 June 2018; published 17 September 2018)

Absolute total, partial, and differential cross sections for the photodetachment of the oxygen anion are reported for photon energies ranging from threshold (1.46 eV) to 5.5 eV. The total cross section was measured using the animated-crossed-beam technique while partial and differential cross sections were obtained using velocity map imaging. The measured values are in good agreement with theoretical results obtained from an R-matrix calculation using polarized pseudostates.

DOI: 10.1103/PhysRevA.98.033410

I. INTRODUCTION

Photodetachment is a tool of choice for studying electron-electron correlations, which are important in weakly bound systems such as anions. In particular, photodetachment of the oxygen negative ion has been studied in some detail for photon energies ranging from threshold (1.46 eV) to the ultraviolet region (7 eV). However, as for most other anions, experimental work is often limited to a single aspect of photodetachment, be it the total cross section or the asymmetry parameter, and restricted to relatively narrow photon energy ranges. The aim of this paper is to present a complete set of absolute measurements of all parameters pertaining to photodetachment, i.e., total, partial, and differential cross sections, performed over a continuous photon energy range spanning the region from 1.46 to 5.5 eV. Such a study is made possible by combining the animated-crossed-beam technique [1,2], velocity map imaging [3], and a tunable optical parametric oscillator (OPO) laser system.

The total cross section σ was first determined in the pioneering work of Branscomb *et al.* [4], followed by additional studies by Smith [5] and Branscomb *et al.* [6]. Later measurements provided additional cross sections for photon energies below 3 eV [7–9]. The total cross section has also been calculated in a fairly large number of theoretical studies [9–19], although both its shape and magnitude vary greatly, and most calculations disagree with the measured values. As highlighted by previous authors [8], such a discrepancy is unsatisfactory since most measurements of the photodetachment cross section for anions are relative, and put on an absolute scale using the O^- cross section of [4–6], as in the case of photodetachment of C^-, B^-, or O_2^- [20–23].

The total cross section above the $1s^2 2s^2 2p^4\ {}^1D$ first excitation threshold, where a steep rise is expected due to channel opening, has only been measured by Branscomb *et al.* [6]. Again, a pronounced disagreement exists between theory and experiment, and also between different calculations [12,16–18]. This photon energy range (above 3.43 eV) has been harder to reach experimentally since tunable UV laser sources were either not available or of excessive complexity.

Above the first excitation threshold, the only experimental work is that by Domesle *et al.* [24] on branching ratios and asymmetry parameters for a photon energy of 4.66 eV, while theoretical results are limited to partial cross sections $\sigma_{^3P}$ and $\sigma_{^1D}$ [11,13,16,25].

The differential cross section $d\sigma/d\Omega$ provides the most detailed information on O^- photodetachment. In the case of linearly polarized light, within the dipole approximation and for an unpolarized target, it can be described by a single asymmetry parameter β:

$$\frac{d\sigma}{d\Omega} = \frac{\sigma}{4\pi}[1 + \beta P_2(\cos\theta)], \tag{1}$$

where P_2 is the Legendre polynomial of order 2 and θ is the angle between the polarization axis of the light and the photoelectron velocity. The behavior of the asymmetry parameter as a function of the photoelectron energy was studied by Cooper and Zare [26], leading to their well-known eponymous formula. At intermediate electron energies, they were able to demonstrate the presence of a broad interference effect between the outgoing s and d waves which manifests itself by a strongly asymmetric emission, perpendicular to the laser polarization. This effect has been confirmed by all subsequent experiments [27–29]. In stark contrast to the total cross section, agreement is excellent between theory [9,26,29] and experiment in the photon energy range covered by the experiments (1.46–2.7 eV). Data above the $O(^1D)$ threshold is limited to the work of Domesle *et al.* [24] and to the best of our knowledge no theoretical values for β have yet been published.

In what follows, we present an absolute measurement of the total cross section, performed using the animated-crossed-beam (ACB) technique of Defrance *et al.* [1] which we

*Present address: Laboratory of Physical Chemistry, ETH Zurich, CH-8093 Zurich, Switzerland.

†xavier.urbain@uclouvain.be

recently adapted to the case of laser-atom interactions [9,30]. Branching ratios and hence partial cross sections were measured using a purpose-built velocity map imaging (VMI) spectrometer, originally developed by Eppink and Parker [3]. Finally, differential cross sections were obtained by measuring the β parameter with the same VMI spectrometer. Effects of the fine structure of both O^- and O were also studied close to thresholds. The results are compared with those of an R-matrix calculation employing polarized pseudostates, as well as with those of earlier work.

The structure of the paper is as follows: The experimental setup for measuring the total cross section is presented in Sec. II along with a brief presentation of the animated-crossed-beam technique; the velocity map imaging setup and the corresponding data analysis procedure are presented in Sec. III; the R-matrix method and computational details are given in Sec. IV; the results are presented and discussed in Sec. V.

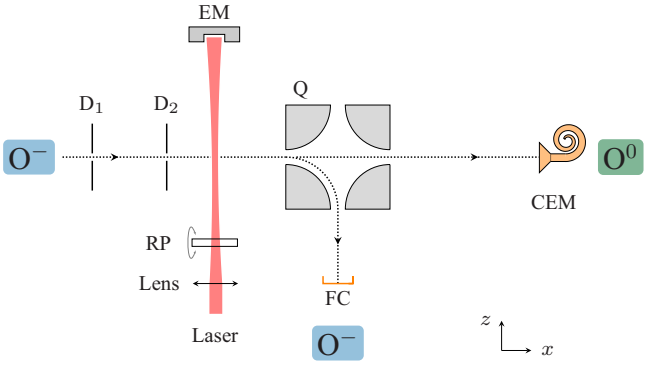

FIG. 1. Sketch of the experimental animated-crossed-beam setup. D_1: circular collimator (diameter 1 mm); D_2: rectangular collimator (100 μm × 1 mm); Q: quadrupolar electrostatic deflector; FC: Faraday cup; CEM: channel electron multiplier; RP: rotating glass plate; EM: energy meter.

II. ANIMATED-CROSSED-BEAM EXPERIMENT

Measuring absolute cross sections is an arduous enterprise since it requires many parameters to be accurately determined and constantly monitored. The major difficulty lies in delimiting the so-called interaction volume, i.e., the spatial and temporal regions where the ion and the laser beam overlap, and thus where photodetachment occurs. Within the interaction volume, the spatial and temporal profiles of the two beams are responsible for local variations of the experimental conditions such as the laser intensity and the ion density. In order to retrieve σ from the experimental data, the beam profiles should in principle be continuously measured. Such measurements are, however, far from easy or accurate since they must be performed *in vacuo* for the ion beam, and involve rather high intensities for the laser beam. In order to circumvent this issue, most experiments assume that the laser beam has a Gaussian spatial profile, justified by a near-TEM_{00} operation, and that the current density of the ion beam is uniform, justified by collimation applied upstream. The actual profiles, however, may depart from such assumptions, introducing discrepancies that render the absolute measurement less reliable.

The animated-crossed-beam technique dispenses with the need to make assumptions about the profiles of the interacting beams and thus facilitates reliable absolute cross-section measurements. The technique was originally developed by Defrance *et al.* [1,2] for electron-impact ionization experiments, and over the past few years we have adapted it to the case of photodetachment. The technique was validated on the H^- anion, for which we obtained excellent results [30], and was also applied to the photodetachment of O^- [9], although over a photon energy range much narrower than that of this study. It has already been described in some detail both for the case of continuous wave (cw) lasers and continuous ion beams [30], and for the case of pulsed ion and laser beams [9]; here, we shall outline only its major features.

The animated-crossed-beam technique relies on vertically sweeping the laser beam across the ion beam and measuring the photodetachment rate N as a function of the laser vertical position Y. Doing so eliminates the need to accurately determine the local, instantaneous ion and photon fluxes, and, under the assumption that photodetachment occurs in the linear regime, the total cross section is given by

$$\sigma = \frac{1}{\eta}\frac{\hbar\omega}{E_{\text{laser}}}\frac{\mathrm{e}v}{I_{\text{ion}}}\int dY\, N(Y), \tag{2}$$

where E_{laser} is the laser pulse energy, I_{ion} is the ion beam current, η is the detection efficiency, v is the velocity of the ions, $\hbar\omega$ is the photon energy, and e is the elementary charge.

The experimental setup, sketched in Fig. 1, is similar to that used in our previous experiments [9,30]. The only change is in the light source, which has been replaced by a pulsed OPO laser system whose wavelength can be continuously tuned from 2600 to 225 nm. Briefly, a beam of oxygen anions is produced in a duoplasmatron source, mass selected by a permanent magnet and accelerated to 5 keV. After collimation by a 1-mm circular diaphragm and a 100 μm ×1 mm slit, the anion beam is intersected at right angles by the light pulses from the OPO. The photodetached oxygen atoms fly in straight lines to a channel electron multiplier (CEM) located downstream, while the remaining negative ions are deflected by a quadrupolar deflector and collected in a Faraday cup (FC) in order to measure the ion current I_{ion}. Note that an electrostatic deflector located before the diaphragms is switched on and off so as to pulse the ion beam and limit the number of background atoms hitting the CEM, hence limiting CEM aging. A duty cycle of 10% is chosen in order to maintain sufficient beam intensity so that the beam current can be precisely measured. The neutral atoms are detected in coincidence with the laser pulses, which reduces background counts to less than 1% of the total signal. Alignment between the collimators and the CEM was carefully checked in order to ensure 100% transmission and collection of the neutrals. The CEM detection efficiency η is estimated to be 95% [9]. The counting rate is kept well below 1 atom per laser shot so as to avoid large corrections during the data analysis due to the Poisson distribution of the events.

The light originating from the OPO is focused onto the anion beam by a lens with focal distance $f = 40$ cm. It enters and leaves the vacuum chamber through laser windows, and is collected on the other side by a pulse energy meter. The

beam is "animated" by a tilted glass plate mounted on a high-accuracy rotation stage and placed just after the lens. Changing the vertical tilt angle results in a well-controlled vertical displacement that must follow the Snell-Descartes refraction law. We verified that this is indeed the case by imaging the transverse profile of the laser beam at the lens focus with a beam-profiling camera and recording its vertical position for a series of different tilt angles and for different wavelengths. Changes in the refraction index with wavelength are taken into account when computing the vertical displacement from the tilt angle. All the optical elements used are coated with broadband antireflection (AR) coatings, and several sets of optics with different AR coatings were needed to span wavelengths ranging from 225 to 860 nm. For most wavelengths, the laser pulse energy measured before and after the exit laser window was identical within the accuracy of the energy meter, demonstrating that transmission losses due to absorption and reflection on the window are negligible. The measured laser pulse energy is therefore the one experienced by the ions inside the vacuum chamber. However, in the ranges from 225 to 250 nm and from 330 to 410 nm, losses of the order of 1% to 3% were observed, and the measured cross sections were corrected accordingly. In the former range, subsequent measurements performed with another window, which exhibited no losses within the accuracy of the energy meter, yielded cross sections in agreement with those measured earlier with a window exhibiting imperfect transmission and appropriately corrected.

A typical experimental run consists in three nested loops. For a given vertical position of the laser beam and a given wavelength, the atoms are counted in coincidence with the laser pulse, the background events are counted in coincidence with another signal of the same duration but shifted in time, and the laser pulse energy and the ion current are measured. Data are acquired in a pulse-by-pulse fashion and subsequently summed or averaged. The glass plate is then rotated to another angle, i.e., the laser beam is moved to another vertical position. During a vertical scan, the glass plate is typically moved by 25 evenly spaced steps and the spacing between steps is chosen so that the ion and laser beams do not overlap at both ends of the scan. The scan is repeated five times in order to improve statistics. Finally the laser wavelength is changed and the whole measurement procedure is repeated. Wavelength scans usually consist of 3 to 10 wavelengths, with the corresponding wave numbers spaced by a constant step of 500 cm^{-1}. In order to secure good statistics and ensure reproducibility, the wavelength scans were run several times, at different times of day and over different days. We measured the absolute photodetachment cross section at 96 different wavelengths, which required the experiment to be run for 41 days.

The whole setup is servocontrolled by a computer, and data acquisition is performed by a DAQ connected to the same computer. For each tilt angle of the glass plate, the position Y_i of the laser beam is retrieved using the Snell-Descartes law. The number of background events $B(Y_i)$ counted during n_s laser shots (typically $n_s = 120$) is subtracted from the number $N(Y_i)$ of neutrals. The pulse energy $E_{\text{laser}}(Y_i)$ and the ion current $I_{\text{ion}}(Y_i)$ are taken as the average of the values measured during the n_s laser shots. Integration of the signal over the vertical position Y of the laser beam is performed numerically using Simpson's rule. The final cross section is the average of cross sections obtained for all scans performed at a given wavelength and the statistical uncertainty is taken as twice the standard deviation.

III. VELOCITY MAP IMAGING EXPERIMENT

Partial and differential photodetachment cross sections can be obtained by measuring the branching ratios R between the various final atomic levels and the asymmetry parameters β for each final level. While the total cross section can be obtained by measuring the production rate of neutrals, i.e., by counting atoms, the measurement of these other quantities requires photoelectron spectroscopy. Early angle-resolved photodetachment experiments were performed using energy analyzers with low solid angle acceptance, and angular distributions were obtained by rotating the laser polarization with a $\lambda/2$ plate [27,28]. Such systems have good energy resolution, but the use of electrostatic analyzers and the need to rotate the laser polarization significantly lengthen measurement times. The velocity map imaging (VMI) technique developed by Eppink and Parker [3] allows the full velocity and angular distributions of the photoelectrons to be recorded in a single measurement. This results in faster acquisition times, and velocity map imaging has therefore become the method of choice in recent experiments [31,32].

A. Experimental setup

We have purpose-built a velocity map imaging (VMI) spectrometer for measuring low-energy photoelectrons. The design of the electrostatic lens is taken from León *et al.* [33], who carefully adjusted the lens dimensions and added guarding and shielding electrodes in order to optimize focusing, resulting in one of the best resolutions available with $\Delta E/E = 0.5\%$. The reason for this choice is that, while we are not attempting to measure high-resolution photoelectron spectra, the full size of the detector cannot be used due to the high speed of the beams, which thus degrades the energy resolution. The design of León *et al.* was therefore chosen in order to maintain good resolution even for small images while limiting the complexity of the system, with some modifications described below.

A schematic view of the setup is presented in Fig. 2. As in the previous experiment, oxygen anions are produced in a duoplamastron source fed with N_2O gas, mass selected, and accelerated to 5 keV. In order to lower the number of background electrons, mainly arising from collisions between anions and the residual gas, and hence limit detector aging, the anion beam is pulsed by switching on and off a deflector (D_1) using a fast, high-voltage switch. When the deflector is off, the ions fly straight to a Faraday cup (FC) and the ion current can be monitored. When the deflector is on, ions fly through the chicane (D_1 and D_2) and are collimated by two diaphragms of diameter 2 and 1 mm, respectively, housed in a rereferencing tube. The deflector is switched on for about 400 ns and its delay with respect to the laser pulse is chosen so that the center of the ion bunch reaches the center of the VMI at the same time as the laser pulse.

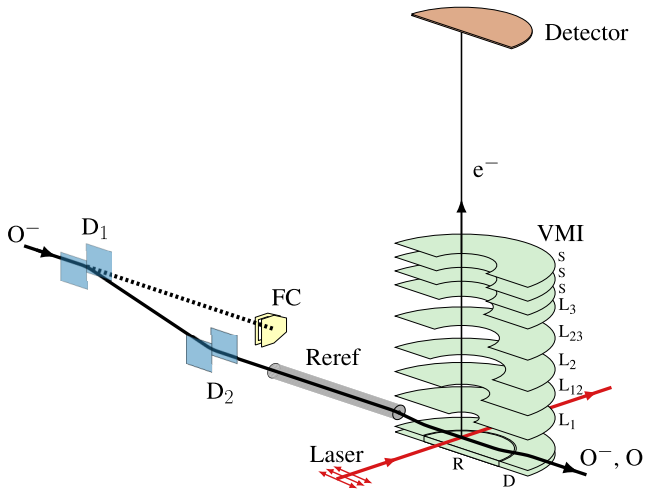

FIG. 2. Schematic view of the velocity map imaging experiment. D_1 and D_2: electrostatic deflectors; FC: Faraday cup; Reref : rereferencing tube; VMI: velocity map imaging spectrometer. Electrodes R, D, L_1, L_{12}, L_2, L_{23}, and L_3 are discussed in the text, S are shielding electrodes. The detector consists of a stack of multichannel plates, a phosphor screen, and a CMOS camera.

The fast anion beam enters the VMI perpendicular to the lens axis. Photoelectrons are emitted within the interaction region at the center of the VMI, where the anion beam crosses the laser beam at right angles. They are extracted towards the detector, perpendicular to the laser-ion plane, by an electric field of typically 50 V/cm, created by the repeller and extractor electrodes. This geometry, together with the use of fast beams, necessitates two modifications of the original lens design. First, the ion beam traveling through the VMI is substantially deflected by the extraction field and, in order to compensate for that deflection, the repeller electrode is split into two concentric disks, as in the setup of Johnson *et al.* [34]. The inner disk acts as the standard repeller electrode, providing a homogeneous extraction field to repel photoelectrons. The outer disk serves as a deflector which counteracts the upwards deflection above the inner disk by downwards deflection before and after. The deflector voltage can be adjusted so that the anions exit the VMI on the same trajectory as they entered. The exiting anions are collected downstream in a Faraday cup and the deflector voltage is optimized by maximizing the measured current. The second modification is prompted by the fact that photoelectrons are emitted within the moving frame of the anions and their velocity in the laboratory frame is therefore the vectorial sum of the photoelectron velocity and the velocity of the anions. As a result, photoelectrons are emitted more off axis than in the case of slow particles or collinear injection and the diameter of the aperture in the extracting electrode had to be enlarged to 20 mm from 14 mm in the original design.

The voltage V_R on the repeller electrode (R) ranges from -150 V for low-energy photoelectrons ($E < 100$ meV) to -1200 V for 4-eV photoelectrons. For each value of V_R, the voltages V_1 and V_2 on L_1 and L_2 are optimized so as to obtain reasonable energy resolution. We found that, in most cases, setting $V_1 = 0.89V_R$ and $V_2 = 0.55V_R$ meets our present needs. Guarding electrodes are set to $V_{12} = (V_1 + V_2)/2$ for L_{12} and $V_{23} = V_2/2$ for L_{23}. The L_3 and shielding (S) electrodes are grounded. The voltage on the deflector (D) is less negative than that of L_1 and is optimized on the measured ion current. It is subsequently adjusted in order to maximize the photoelectron signal.

Along with these modifications of the original VMI design, we have added a rereferencing tube in order to minimize adverse effects due to the deceleration of ions as they enter the VMI lens. As the ion bunch flies through the tube, the latter is rapidly switched from the ground to a high voltage lying between that of the deflector and L_1. This effectively rereferences the ion bunch from the ground to the VMI voltage and, when the ions exit the tube, the potential gradient at the VMI entrance is almost suppressed and deceleration strongly reduced. We note, however, that for our high beam energy (5 keV) and relatively low VMI voltages (-150 to -1200 V), we have seen no particular improvement on the energy resolution when the rereferencing tube is used.

Since screening of magnetic fields is critical for photoelectron spectroscopy, the VMI lens and flight tube are surrounded by two concentric μ-metal shields. The repeller electrode is manufactured with ARCAP non-magnetic alloy, while all other electrodes are made of nonmagnetic stainless steel. The setup is placed in a stainless steel chamber pumped to high vacuum (10^{-8} mbar).

Light pulses are produced by the OPO laser system used for the animated-crossed-beam experiment described above. At the exit of the OPO, light passes through a $\lambda/2$ plate and a polarizing beam splitter. This combination provides control over the laser pulse energy and sets the polarization of the light parallel to the plane of the imaging detector. In the infrared and visible range, light is focused by an $f = 40$ cm lens onto the anion beam at the center of the VMI. It enters and leaves the vacuum chamber through laser windows. All optics are AR coated.

In the ultraviolet range, scattered photons hitting the VMI electrodes, in particular the repeller, are an important source of background photoelectrons which, in turn, strongly affect the measured images. In order to reduce the background as much as possible, we placed a series of baffles along the laser beam path, 10 before the entrance of the VMI and 5 after. Each baffle has a 4-mm hole at its center, where light passes through, and is coated with colloidal graphite to reduce reflection. The μ-metal shields are also coated with colloidal graphite. In addition, the $f = 40$ cm lens was removed and the laser windows were tilted at an angle to prevent light reflected onto the (AR-coated) windows from penetrating inside the VMI. For wavelengths below 280 nm, we also replaced the repeller electrode by a grid with 90% transparency and a positively biased plate located $\sim$5 mm underneath. This design strongly reduces the number of background photoelectrons [34,35] while maintaining good focusing properties. Note that the positive bias on the plate must be kept low enough, roughly 300 V higher than the repeller voltage, in order not to modify the electrical potential seen by the photodetached electrons in the interaction region.

Photoelectrons are imaged onto the COBRA position-sensitive detector [36], which consists of a stack of two

microchannel plates (MCP), a waveform digitizer, a phosphor screen, and a CMOS camera. The arrival time of photoelectrons at the detector can be measured by COBRA but this is not required in this study and therefore not recorded. Injecting the anion beam perpendicular to the VMI axis yields a detection system simpler than that used for collinear injection [31,33], where voltage on the MCP must be rapidly lowered before the ion pulse hits the detector. Measurements are performed at 30 Hz, the repetition rate of our laser, and images are processed in real time. Each image is 512×512 pixels in size and the position of each electron hit is determined with subpixel accuracy using a centroiding algorithm. On average, we work with 3 or 4 electrons per laser shot and data for each wavelength are acquired until about 100 000 events are recorded.

B. Data processing

The raw images measured with the present setup are typical of velocity map imaging experiments and show an arrangement of concentric disks with bright edges, each corresponding to a given photoelectron velocity. The angular distribution of electron impacts across the disks is reminiscent of the photoelectron angular distribution. In the present case, the center of the disks is shifted with respect to the center of the detector by the ion velocity, preventing us from using the full size of the detector. For an anion velocity of 2.5×10^5 m/s, the shift amounts to about 20% of the velocity of 4-eV photoelectrons, and thus 20% of the distribution's radius. For 0.15-eV photoelectrons, the shift reaches 100% of the distribution's radius. The raw image is slightly distorted, an effect we ascribe to the presence of a small, residual magnetic field due to imperfect magnetic shielding of the spectrometer, and small inhomogeneities of the electric field inside the detachment region. The image must therefore be circularized prior to Abel inversion.

Circularization is based on the observation that the two-dimensional (2D) projection of the Newton sphere on the detector appears rotated and sheared, hence producing, instead of a perfect circle, an ellipse with principal axes at an angle with respect to the horizontal and vertical axes of the image. Note that this deformation is small, and the relative difference between the minor and major axes is of the order of 5% or less. The two deformations can be parametrized with only two quantities, the rotation angle ϕ and shearing factor γ, which can be extracted from the image itself by determining the major and minor axes of the ellipse and their orientation with respect to the horizontal axis. To do so, one first needs to express the coordinates of the electron impacts, hereafter referred to as events, in terms of polar coordinates (r, θ). The radius r_e of the bright outer edge of each ellipse, related to the photoelectron velocity, must then be determined for all angles θ. In practice, we obtain a set of radial positions $r_e(\theta_i)$ by fitting the radial distribution of events contained within consecutive angular slices $[\theta_i, \theta_{i+1}]$ with the Abel transform of a set of Gaussian functions whose widths and centers are fit parameters. The positions $r_e(\theta_i)$ are then fitted to an ellipse equation and the deformation parameters ϕ and γ readily extracted. Finally, the new Cartesian coordinates (x', y') of all events are calculated from the original ones (x, y) using

$$x' = x\cos\phi + y\sin\phi - \gamma(-x\sin\phi + y\cos\phi), \tag{3}$$

$$y' = -x\sin\phi + y\cos\phi, \tag{4}$$

so as to correct the deformations.

For photon energies above roughly 4 eV, photoelectrons produced by stray photons at the surface of the electrodes give rise to a significant background in the VMI images. To correct for this background, we also recorded images in absence of the O^- beam, i.e., in the absence of signal. The background images are smoothed by convolution with a uniform, 3×3 matrix, and used to estimate the rate of background events λ_b at each image pixel. They then serve to eliminate background in images taken when the O^- beam is present. To do so, it suffices to compute, for each pixel, the best estimate $\bar{s}$ of the number of signal events, given by

$$\bar{s} = \sum_{k=0}^{m} k\frac{(\lambda_b)^{m-k}e^{-\lambda_b}}{(m-k)!}, \tag{5}$$

from the total number m of events recorded at the pixel and the background rate λ_b. The above formula takes into account the Poisson distribution of the events.

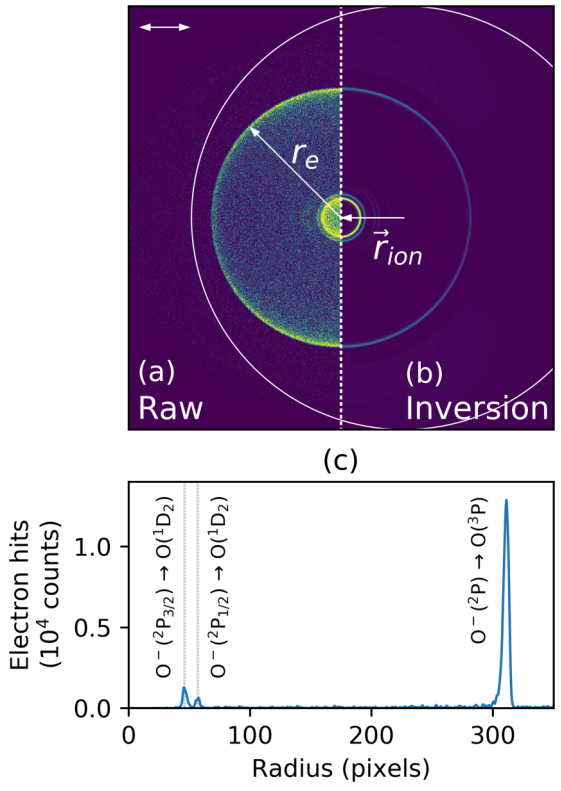

FIG. 3. Data for the photodetachment of O^- at $\lambda = 357.14$ nm (3.47 eV). (a) Circularized raw image (1024×1024 pixels). The horizontal arrow indicates the direction of the laser polarization. (b) Inverse-Abel transform image computed with MEVELER. The large outer circle is the edge of the detector. r_e is the radius of the bright outer edge of the image, $\vec{r}_{ion}$ is the shift of the image center with respect to the center of the detector due to the ion beam velocity. (c) Radial distribution of the electrons after Abel inversion.

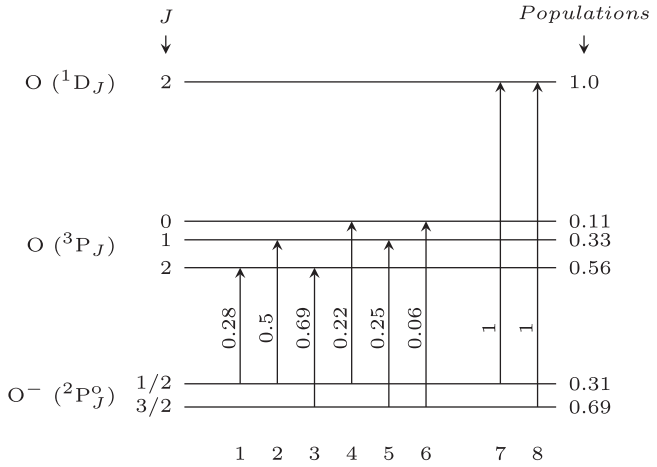

FIG. 4. Sketch of the fine-structure energy levels of O^- and of the ground and first excited levels of O. Transitions, depicted by the arrows, are numbered by increasing energy. The arrow labels are the theoretical fine-structure branching ratios [see Eqs. (13) and (14) in Sec. V B]. The initial and final populations, obtained from experimental transition intensities and theoretical branching ratios, are indicated on the right. The sketch is not to scale.

After circularization, the inverse Abel transform of the processed images is computed using the MEVELER code of Dick [37], which provides good resolution, noise resistance, and excellent behavior even for low numbers of events. Circularization parameters are further refined by iterating the circularization and Abel inversion procedures and minimizing the square of the residuals between the corrected experimental image and the VMI image produced by the inversion algorithm.

Figure 3 shows an example of measurement and data processing for $\lambda = 357.14$ nm. The left half of the upper image is the circularized image, the right half is the Abel inverted image, and the bottom graph is the radial distribution of photoelectrons. Three different electron velocities are observed, which we can straightforwardly attribute, from left to right, to the fine-structure transitions from O^- to $O(^1D)$ (transitions 8 and 7 in Fig. 4), and O^- to $O(^3P)$ (transitions 1 to 6). The six different transitions between the fine-structure components of O^- and $O(^3P)$ are not resolved.

The intensity of the transitions to $O(^3P)$ and $O(^1D)$ is obtained by fitting the peaks in the velocity distribution with Gaussian functions and computing the area $\mathcal{P}_{^3P}$ under the rightmost peak and the area $\mathcal{P}_{^1D}$ under the two leftmost peaks. The branching ratio between $O(^3P)$ and $O(^1D)$ can then be obtained using

$$R_{^1D} = \frac{\mathcal{P}_{^1D}}{\mathcal{P}_{^1D} + \mathcal{P}_{^3P}}. \tag{6}$$

For the distribution presented in Fig. 3, we obtain $R_{^1D} = 0.102 \pm 0.007$, where the uncertainty is the 1σ standard deviation computed from the relevant covariance matrix elements.

The asymmetry parameter β for each final term is given by the ratio between the $Q_2(r)$ and $Q_0(r)$ radial distributions calculated by the MEVELER program [37]. When divided by r^2, they represent the contributions of the Legendre polynomials of order 2 and 0 to the total angular distribution. This ratio is of course only meaningful where Q_0 has sufficient intensity, and we observed that the accuracy on the determined β rapidly degrades as Q_0 becomes lower. Therefore, the average value of β for a given peak is calculated by considering the experimental points for which Q_0 is higher than typically 10% of the peak maximum and with a weighting factor of Q_0^2. For the velocity distribution presented in Fig. 3, we obtain $\beta_{^3P} = -0.54$ and $\beta_{^1D} = -0.11$.

The accuracy $\Delta\beta$ on the asymmetry parameter is in principle limited by the angular resolution of the detection system, given by $\Delta\theta = 1/r_e$ with r_e the radius, in pixels, of the Newton sphere on the image. In our setup, the value of $\Delta\theta$ typically lies between 0.2° and 0.6°. However, the image circularization and the Abel inversion procedures cause further uncertainties which increase $\Delta\beta$ up to an estimated value of 0.035. In order to assess the absolute accuracy of the VMI apparatus and data acquisition and analysis methods, we have measured the asymmetry parameter for the photodetachment of the H^- ion at photon energies of 1.31 and 1.77 eV. The experimental values are, respectively, $\beta = 1.995\,^{+0.005}_{-0.035}$ and $\beta = 1.994\,^{+0.006}_{-0.035}$, in excellent agreement with the value of $\beta = 2$ predicted by theory and confirmed experimentally at higher photon energies [27].

Although not essential for this study, the energy resolution $\Delta E/E$ is of the order of 2% for the largest images and when potentials on the VMI electrodes are carefully optimized. We did not optimize potentials for each repeller voltage, thus resolution fluctuates from 2% to 4% throughout the measurements. It also degrades close to thresholds, where photoelectron velocities are low and images become small. Although the present resolution does not reach the 0.5% resolution of León *et al.* [33], it is considered satisfactory since the ion beam velocity prevents us from using the full detector size. Enhancing the magnetic shielding and reducing the velocity spread of the ion beam may further enhance the resolution for future studies.

IV. THEORY

Photodetachment cross sections and asymmetry parameters were calculated using standard, nonrelativistic R-matrix theory as implemented in the UK APAP (Atomic Processes for Astrophysical Plasmas) suite of computer codes [38]. The general method for photoionization is described in detail in Chap. 8 of [39]. Here, we recall only the main features that are necessary for understanding the various parameters used in the calculations.

The Schrödinger equation is solved by partitioning the configuration space of the $N+1$ electrons of O^- into two regions. The inner region is characterized by the radial boundary a beyond which the charge distribution of all states of the residual oxygen atom retained in the calculation is vanishingly small. In this region, correlations between all electrons are important. The wave function of the system is expanded in a basis of configuration interaction (CI) wave functions for oxygen coupled to a set of continuum orbitals describing the ejected electron and satisfying a one-electron Schrödinger equation with a zero-derivative boundary condition at $r = a$. The basis is supplemented by a number of $(N+1)$-electron "bound" configurations that vanish at $r = a$, which account

TABLE I. Parameters of the first nine Slater orbitals optimized on the energy of O($1s^2 2s^2 2p^4$) ^3P and ^1D using the computer code CIV3.

	$C_{j n\ell}$	$I_{j n\ell}$	$\zeta_{j n\ell}$		$C_{j n\ell}$	$I_{j n\ell}$	$\zeta_{j n\ell}$
$1s$	39.33603	1	7.62035	$2p$	2.98746	2	1.82324
	3.83917	1	13.38030		8.32283	2	3.46668
	0.05886	2	3.15190		0.29042	2	1.15634
	4.50779	2	6.45968		2.95902	2	7.73305
	−0.00045	2	1.88150				
				$\bar{3}p$	5.83101	2	2.06590
$2s$	−9.20444	1	7.62035		−1.22828	3	1.27355
	−0.58928	1	13.38030				
	9.99260	2	3.15190	$\bar{4}p$	9.48240	2	2.24938
	−12.89749	2	6.45968		−39.65146	3	2.48231
	3.53407	2	1.88150		0.45064	4	1.43223
$\bar{3}s$	13.29458	1	3.61049	$\bar{3}d$	11.07440	3	2.54412
	−52.00070	2	3.32207				
	12.99921	3	2.34723	$\bar{4}d$	47.64679	3	2.34370
					−60.38147	4	2.72177
				$\bar{4}f$	15.10271	4	2.96966

for short-range correlations, necessary for describing bound states and resonances of the negative ion. The expansion coefficients are determined by diagonalizing the $(N+1)$-electron Hamiltonian in this basis. In the outer region, the photoelectron moves beyond $r = a$ while the others remain bound. Neglecting exchange with the bound electrons, the interaction of the photoelectron with the residual atom can be written as a multipole potential. The wave function for the system is represented by a standard close-coupling expansion involving products of atomic wave functions and a set of as yet unknown functions describing the photoelectron. These functions satisfy second-order coupled differential equations, with appropriate asymptotic boundary conditions for the initial, bound state of the anion or the final states of the residual atom plus photoelectron. The initial and final states are determined by matching the inverse logarithmic derivatives of the solutions in the inner and outer regions at their common boundary $r = a$. The photodetachment cross section is then computed from the dipole matrix elements between the initial and final

TABLE II. Parameters of the three additional polarized pseudo-orbitals optimized on the polarizability of O($1s^2 2s^2 2p^4$) ^3P using the computer code CIVPOL.

	$C_{j n\ell}$	$I_{j n\ell}$	$\zeta_{j n\ell}$		$C_{j n\ell}$	$I_{j n\ell}$	$\zeta_{j n\ell}$
$\bar{4}s$	5.36028	1	0.62348	$\bar{5}d$	20.15973	3	2.04062
	−38.92513	2	3.02905		−38.16027	4	2.65231
	−0.77018	3	0.88200		0.11302	5	1.37578
	−2.82472	4	1.67166				
$\bar{5}p$	12.25191	2	0.50859				
	−38.27471	3	0.73251				
	37.34929	4	1.36681				
	3.24368	5	0.98600				

TABLE III. Energies of the three terms associated with the $1s^2 2s^2 2p^4$ ground configuration of oxygen. The observed values are taken from the NIST Atomic Spectra Database [47].

	Absolute (a.u.)	Relative (eV)	Observed (eV)
^3P	−74.97396	0.0	0.0
^1D	−74.89971	2.0204	1.9577
^1S	−74.81622	4.2924	4.1803

states of the system, summed over the final and averaged over the initial magnetic and spin projection quantum numbers.

For the range of laser wavelengths and intensities considered here, only the $1s^2 2s^2 2p^4$ ^3P and ^1D states of oxygen can be populated. The radial parts $P_{n\ell}(r)$ of the one-electron orbitals used to build the atomic wave functions are written as a sum of Slater orbitals,

$$P_{n\ell}(r) = \sum_{j=1}^{k} C_{j n\ell} r^{I_{j n\ell}} \exp(-\zeta_{j n\ell} r), \tag{7}$$

where $C_{j n\ell}$, $I_{j n\ell}$, and $\zeta_{j n\ell}$ are variational parameters. In the calculations presented here, the set of orbitals includes the $1s$, $2s$, and $2p$ Hartree-Fock orbitals given by Clementi and Roetti [40], together with $\bar{3}p$, $\bar{4}f$, $\bar{3}d$, $\bar{3}s$, $\bar{4}p$, and $\bar{4}d$ correlation orbitals optimized successively on the energy of $1s^2 2s^2 2p^4$ ^1D using the atomic structure computer code CIV3 [41]. All configurations formed through single and double excitation of the $n = 2$ shells of the ground configurations are included. The CIV3 orbitals are supplemented with $\bar{4}s$, $\bar{5}p$, and $\bar{5}d$ orbitals, whose Slater parameters were determined by optimizing on the polarizability of the oxygen ground state using the computer package CIVPOL [42], an extension of CIV3. The Slater parameters of the orbitals are given in Tables I and II, while the energies of the first three levels of oxygen are presented in Table III. The value of the ^1D threshold with respect to the ground level ^3P is 2.0204 eV, significantly better than the value of 2.1946 eV in our previous work [9] which was limited to photodetachment below the ^1D threshold.

The full averaged polarizabilities of the ground and first excited states are presented in Table IV. They are computed from the dipole matrix elements with three coupled polarized pseudostates [42], respectively $\overline{^3S^o}$, $\overline{^3P^o}$, $\overline{^3D^o}$ and $\overline{^1P^o}$, $\overline{^1D^o}$, $\overline{^1F^o}$. The full averaged polarizabilities of the ^3P states, 4.83 a_0^3, lies within the error bars of the experimental value [43] and is about 10% smaller than the value obtained in the CASPT2 (second-order complete active space perturbation theory) calculations [44,45]. We note that in our previous work [9], we used a much simpler Hartree-Fock wave function for the oxygen ground state, with three coupled polarized pseudostates. These gave a polarizability of 5.08 a_0^3, in better

TABLE IV. Full averaged polarizabilities of the $1s^2 2s^2 2p^4$ ^3P and ^1D states of oxygen, in a_0^3.

	CIVPOL	CASPT2 [45]	Measured [43]
^3P	4.83	5.35	5.2 ± 0.4
^1D	4.84	5.43	–

agreement with the experimental value despite the fact that the atomic wave functions were in principle less accurate. Our value for the polarizability of the ^1D first excited state is very similar to that for the ground state, and lies within 11% of the CASPT2 result [44,45], even though the three polarized pseudoorbitals are not optimized for this case.

In the R-matrix calculations, we set the size of the inner region to 35 a_0, sufficient to ensure that the amplitudes of all the orbitals have decayed to less than 1×10^{-3} at the boundary, and take 30 continuum orbitals per angular momentum to represent the photoelectron. We include the three target states corresponding to the $1s^22s^22p^4$ ground configuration and the six polarized pseudostates mentioned above to account for the polarizabilities of the ^3P and ^1D states. The calculation yields an electron affinity for O of 1.47 eV, slightly larger than the difference of 1.46 eV between the weighted average of the experimental fine-structure levels of the ground multiplets for $O^-(^2P^o)$ [46] and $O(^3P)$ [47]. We note that the corrections to the NIST values [47] given by [48] are quite small, and do not change the experimental electron affinity to the level of precision quoted above.

V. RESULTS AND DISCUSSION

A. Total cross section

The present results for the total photodetachment cross section of O^- are shown in Fig. 5 and compared against available experimental data [5–9]. The measurements cover photon energies from 1.46 to 5.51 eV in steps of 0.062 eV (500 cm^{-1}), with even smaller steps close to thresholds, thus extending by more than 1.5 eV the range over which experimental data are available. The error bars shown in Fig. 5 represent the 2σ statistical uncertainty, where σ is the standard deviation. Uncertainties arising from systematic effects are listed in Table V and, when added in quadrature, yield a total systematic uncertainty of 7%.

TABLE V. List of experimental uncertainties arising from systematic effects.

Pulse energy E_{laser}	5%
CEM detection efficiency η [9]	4%
Vertical displacement Y [30]	2%
Ion velocity v [30]	1%
Ion current I_{ion} [30]	1%

The present data are in good agreement with both the measurement of Lee and Smith [7] and our previous measurement [9] in the region close to the $O(^3P)$ threshold. Above 2.2 eV, there is also excellent agreement with our previous experiment performed with cw lasers. The discrepancy previously observed with the results of Smith [5], Branscomb *et al.* [6], and Hlavenka *et al.* [8] remains. A monotonous increase of the cross section is observed above 2.2 eV where previous experiments exhibit a plateau with a slightly negative slope. The possible reasons for this discrepancy have been discussed before [9], however, a definitive explanation remains elusive. This persistent discrepancy certainly calls for further experimental investigation.

The opening of the first ^1D excitation channel manifests itself as a steep rise in the cross section above 3.43 eV. The present cross section does not match that measured by Branscomb *et al.* [6], which was put on an absolute scale using the data of Smith [5]. As stated by Branscomb *et al.*, calibration of their apparatus was challenging for photon energies above 3.7 eV due to stray photoelectrons produced by UV light on the walls of the vacuum chamber. Detection of these stray photoelectrons may change the observed cross section and, while no uncertainty was given, a difference of more than 2.5×10^{-22} m^2 (25%) between the measured cross section and a crude theoretical estimate was regarded by the authors as noncontradictory [6]. The present results above

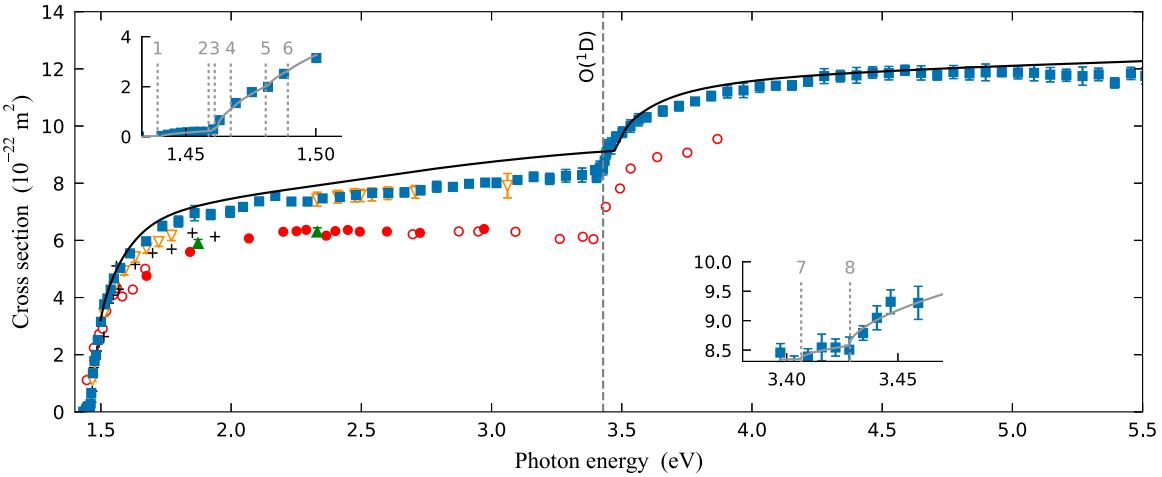

FIG. 5. Total photodetachment cross section of O^-. Full squares: present experiment; full triangles: absolute measurement of Hlavenka *et al.* [8]; open inverted triangles: absolute measurement of Génévriez *et al.* [9]; full circles: absolute measurement of Smith [5]; open circles: relative measurement of Branscomb *et al.* [6]; crosses: absolute measurement of Lee and Smith [7]; full line: present R-matrix calculation in the length form. The vertical dashed line corresponds to the $O(^1D)$ threshold. The insets show results from the present experiment around the $O(^3P)$ and $O(^1D)$ thresholds, from left to right. The vertical dotted lines indicate the position of the various fine-structure thresholds, numbered as in Fig. 4.

the O(^1D) threshold also lie within 25% of the values of Branscomb *et al.* For photon energies above 3.93 eV, no other experimental data are available.

In our previous work [9], we used cw Ar^+ and Ti:sapphire lasers operating in near-TEM_{00} mode which produced a high-quality light beam, with a spatial profile very close to Gaussian and excellent power stability. In the OPO laser system used in this study, light pulses are generated through a series of nonlinear processes in optical crystals and, as a result, the quality of the light beam is greatly deteriorated. The spatial profile is far from Gaussian and varies strongly with the wavelength. Pulse-to-pulse energy fluctuations reach standard deviations of more than 30% and important fluctuations in the time profile of individual laser pulses can also be observed since the Nd:YAG pump laser is multimode. In theory, the animated-crossed-beam technique does not set restrictions on the laser intensity profile, as long as it remains constant throughout a vertical scan of the light beam, and it can very well accommodate the use of pulsed laser beams [9,30]. Moreover, pulse-to-pulse fluctuations in the time profile of the laser pulses can be averaged out by measuring over a sufficiently large number of pulses while monitoring the individual pulse energy, as was done here. The good agreement reached between the present experiment and our previous measurement illustrates the robustness of the animated-crossed-beam technique and hence validates its use with pulsed laser sources.

The insets in Fig. 5 show details of the cross section around the O(^3P) and O(^1D) thresholds. The positions of the various fine-structure thresholds are indicated by the vertical dotted lines, numbered as in Fig. 4, and the most intense fine-structure transitions are observed in the cross-section curve. The region around the O(^3P) threshold has been measured in much greater detail by Neumark *et al.* [49] and Suzuki and Kasuya [50], but reaching such a level of detail was not the primary goal of the work reported here. We also note that electron affinities obtained in [49] have subsequently been revised by Blondel *et al.* [51].

The present experimental results are compared in Fig. 6 with those of our R-matrix calculation using polarized pseudostates as well as with previous theoretical studies. In our calculations, there is very good agreement between the cross sections computed using the length and velocity forms of the dipole matrix elements. The overall agreement with our measured values is quite good, the main differences occurring below the ^1D threshold where the R-matrix results are between roughly 5% and 10% larger. The BSR calculation by Zatsarinny and Bartschat is based on the B-spline R-matrix method (BSR) [17] and includes a large number of accurate target states and pseudostates. The BSR cross sections are about 15% larger than the present measurement below the O(^1D) threshold, but are only 6% higher above the O(^1D) threshold, which puts them outside the 2σ statistical uncertainty indicated by the error bars but within the 7% systematic experimental uncertainty. Agreement with the early work by Robinson and Geltman [12] is surprisingly good below the O(^1D) threshold, considering that their calculation is based on a one-electron model potential adjusted to the experimental electron affinity. Their cross sections above the O(^1D) threshold are, however, much higher than the present measurement.

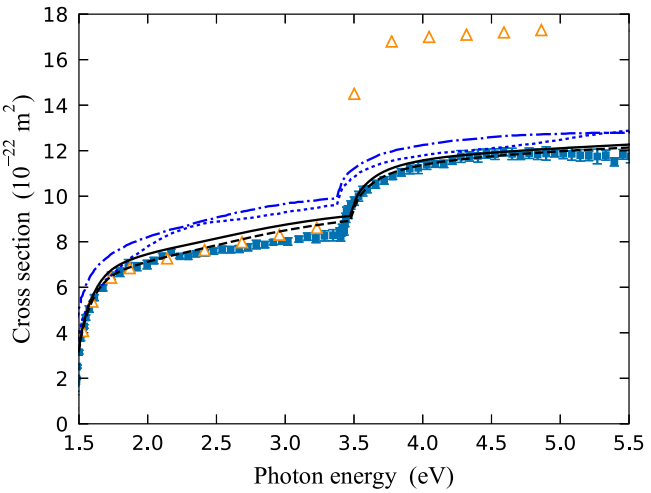

FIG. 6. Total photodetachment cross section of O^-. Full squares: present experiment; open triangles: model potential calculation of Robinson and Geltman [12]; full thick line and dashed line: present R-matrix calculation in the length and velocity gauges, respectively; dotted line and dotted-dashed line: BSR calculation of Zatsarinny and Bartschat [17] in the length and velocity gauges, respectively.

Robinson and Geltman suggested that this discrepancy could be due to the fact that the averaged polarizability of O(^1D) might not be the same as that of O(^3P). They used the same experimental value in their calculations. As shown in Table IV, however, the two polarizabilities are not expected to be that different, so this explanation appears less plausible.

It should also be noted that the photodetachment cross section of O^- has been calculated in a number of other theoretical studies, ranging from semiempirical calculations to equation-of-motion coupled-cluster Dyson orbital or density functional theory calculations [10,13,18,19,25,52]. The results of these calculations differ substantially from the data presented in Figs. 5 and 6 both in shape and magnitude and are thus not presented here.

The cross section at the O(^3P) threshold can be fitted by a sum of Wigner threshold laws [53] associated with each fine-structure transition and including only s-wave contributions since these are predominant for low-energy photoelectrons. A typical fit function takes the form

$$\sigma(\epsilon) \propto \sum_{j=1/2}^{3/2} \mathcal{P}_j \sum_{j'=0}^{2} R_{jj'}(\epsilon - E_{jj'})^{1/2}, \tag{8}$$

where ϵ is the photon energy and $\mathcal{P}_j$ is the initial population of the anion fine-structure component $O^-(^2P_j)$. $R_{jj'}$ and $E_{jj'}$ are the branching ratio and transition energy of the jj' transition from the initial $O^-(^2P_j)$ level to the final O($^3P'_j$) levels. The transition energies are computed using electron affinities and energy levels from [46,48]. Branching ratios $R_{jj'}$ for levels associated with the oxygen ground term O(^3P) have been determined theoretically and experimentally by several authors [31,54,55], and can be computed as shown below. We use these ratios in Eq. (8) to extract the initial populations $\mathcal{P}_j$ of the fine-structure components of O^- from the fit. They are found to be 0.34 ± 0.02 and 0.66 ± 0.02 for the $J = \frac{1}{2}$ and $\frac{3}{2}$ components, respectively.

The partial cross section into O(^1D) close to threshold, discussed in the next section, can be fitted in a similar manner. If we assume that the partial cross section to O(^3P) evolves linearly with photon energy across the O(^1D) threshold, the behavior of the total cross section can then be expressed in the form

$$\sigma(\epsilon) \propto \sum_{j=1/2}^{3/2} \mathcal{P}_j R_{j2}(\epsilon - E_{j2})^{1/2} + a\epsilon + b. \tag{9}$$

The transition energies E_{j2} are computed using [46,47], while the branching ratios R_{j2} to the O($^1D_2$) level are calculated using Eq. (13). The initial fine-structure populations are denoted by $\mathcal{P}_j$, while a and b are fit parameters. The fine-structure populations deduced after fitting are 0.30 ± 0.14 and 0.70 ± 0.14 for $J = \frac{1}{2}$ and $\frac{3}{2}$, respectively, in agreement with those estimated from the fit of the O(^3P) threshold.

B. Partial cross section

The branching ratio $R_{^1D}$ to the O(^1D) final term, obtained from our VMI measurements, is presented in Fig. 7(a). It increases rapidly above threshold and soon reaches a plateaulike region where, on average, photodetachment leaves about 20% of the oxygen atoms in the ^1D term and the rest in the ground term. For a photon energy of 4.66 eV ($\lambda = 266$ nm), the present branching ratio of 0.21 ± 0.02 lies within the uncertainty of the value of 0.24 ± 0.04 measured by Domesle *et al.* [24]. The solid line in Fig. 7(a) represents a fit of the branching ratio using

$$R_{^1D}(\epsilon) = C \sum_{J=1/2}^{3/2} \mathcal{P}_J \frac{(\epsilon - E_{J2})^{1/2}}{1 + b(\epsilon - E_{J2})^a}, \tag{10}$$

where $\mathcal{P}_J$ is the initial population of the Jth fine-structure component of O^- obtained from the analysis of the VMI images (see below), E_{J2} is its energy difference with respect to O($^1D_2$) and a, b, and C are fit parameters. The rationale behind this choice of function is that $R_{^1D}(\epsilon)$ tends to a Wigner threshold law for low photoelectron energies and is almost constant in the high-energy region. While the partial cross section to O(^1D) must follow a Wigner law at threshold, this is not the case for the branching ratio. However, since the partial cross section to O(^3P) remains essentially flat across the O(^1D) threshold region, the partial cross section and branching ratio to O(^1D) exhibit essentially the same behavior and $R_{^1D}$ follows to a good approximation the increase predicted by the Wigner threshold law. The best fit is obtained for $a = 0.61$, $b = 2.07$ eV$^{-0.61}$, and $C = 0.63$ eV$^{1/2}$.

The partial photodetachment cross sections to the O(^3P) and O(^1D) final terms can be deduced from the total cross section and the fit to the branching ratio, i.e.,

$$\sigma_{^1D} = R_{^1D}\,\sigma, \tag{11}$$

$$\sigma_{^3P} = (1 - R_{^1D})\,\sigma. \tag{12}$$

These are shown in Fig. 7(b), together with the total cross section and the theoretical partial cross sections obtained from our R-matrix calculation with polarized pseudostates. Although the theoretical ^1D threshold lies slightly higher than the experimental value, there is very good agreement between the theoretical and experimental ^1D partial cross sections. There is also good agreement between the ^3P partial cross sections above 4 eV.

For a given final term (^3P or ^1D), branching ratios between the various fine-structure components of both the initial anionic term ($J = \frac{1}{2}, \frac{3}{2}$) and the final atomic term can be considered (see Fig. 4). It is well established that these ratios are not a simple product of the statistical weights of the initial and final levels [54,56]. For detachment of a p electron close to threshold, they can be expressed as

$$R_{JJ'} = \frac{G_{JJ'}}{\sum_{J''} G_{JJ''}} = (2L+1)(2S+1)G_{JJ'}, \tag{13}$$

where $G_{JJ'}$ are geometrical factors obtained through angular momentum conservation and coupling between the atomic target and the outgoing photoelectron [55]

$$G_{JJ'} = (2J'+1)\sum_{\lambda}(2\lambda+1)\begin{Bmatrix} L' & S & \lambda \\ \frac{1}{2} & J' & S' \end{Bmatrix}^2 \begin{Bmatrix} L' & S & \lambda \\ J & \ell_0 & L \end{Bmatrix}^2. \tag{14}$$

The quantum numbers (L, S, J) and (L', S', J') are relative to the anion and the atom, respectively, ℓ_0 is the initial orbital quantum number of the electron which is 1 for a p electron.

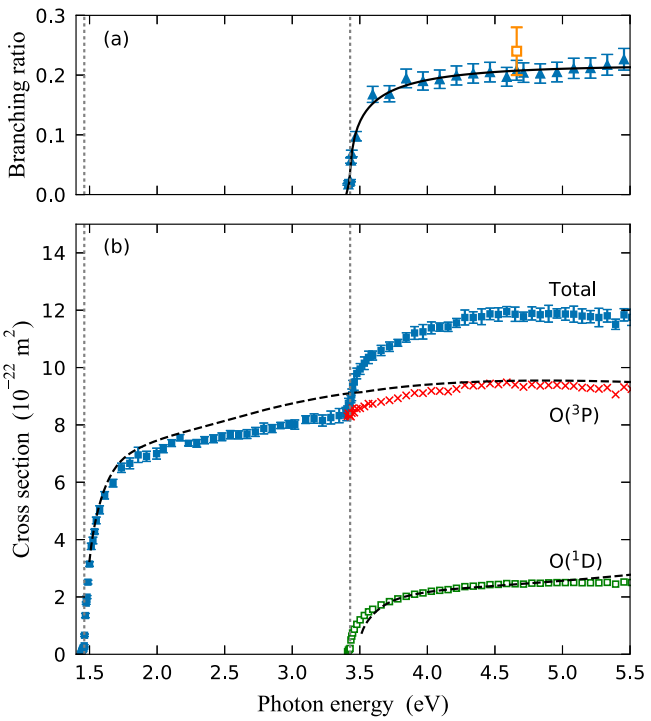

FIG. 7. (a) Branching ratio for the O(^1D) final term and (b) total and partial photodetachment cross sections. (a) Full triangles: present measurement; open square: measurement of Domesle *et al.* [24]; full line: fit of the present data (see text). Uncertainties are 1σ values coming from least-square fitting procedure. (b) Full squares: total cross section; crosses: partial cross section to the O(^3P) term; open squares: partial cross section to the O(^1D) term; dashed lines: partial cross sections from the present R-matrix calculation in the length gauge.

For the oxygen ground term ($J' = 0, 1, 2$), fine-structure branching ratios have been determined experimentally up to photon energies of 2.54 eV and are similar to those obtained from Eqs. (13) and (14) [28,31,32]. The purely geometrical picture is strictly valid only if a single partial wave contributes to detachment [55], as is the case close to threshold where s-wave detachment predominates. However, increasing photon energies see the onset of d-wave detachment and the ratios determined from Eqs. (13) and (14) should not be valid since geometrical factors cannot be separated from radial dipole matrix elements in the various summations involved in the calculation of the cross sections. Pan and Starace [55] showed that the geometrical picture still holds far from threshold if one-electron dipole matrix elements are term independent and Cavanagh *et al.* observed, following their experimental results, that this must be the case for the ground term of oxygen [31,55]. Interestingly, we note that term independence is a characteristic of central potential models, so that the larger range of validity of the geometrical approach may help to explain the excellent agreement between the present measured total cross sections and those of the model potential calculation of Robinson and Geltman below the ^1D threshold [12].

In the present VMI measurement, fine-structure transitions are resolved up to ~0.3 eV above threshold. The transition intensities and the branching ratios can also be obtained by fitting the fine-structure peaks in the photoelectron velocity distribution with Gaussian functions and computing their areas. Experimental branching ratios between transitions from an initial $O^-(^2P^o_J)$ level to the various final levels $O(^3P_{J'})$ match those obtained from the geometrical picture, using Eqs. (13) and (14), to within 15%–20% for the brightest transitions and 30% for the less intense ones. Moreover, since they have been experimentally verified, we use the theoretical branching ratios for the $O(^3P_{J'})$ channels to estimate the initial populations of the fine-structure components of O^-. We obtain populations of 0.69 ± 0.01 and 0.31 ± 0.01 for the $J = \frac{3}{2}$ and $\frac{1}{2}$ components, which agree to within the experimental uncertainty with the populations determined by fitting the total cross section close to the $O(^3P)$ and $O(^1D)$ thresholds (see Sec. V A). Identical values are obtained when considering data close to the $O(^1D)$ threshold, albeit with an uncertainty that is twice larger (0.02).

The measured fine-structure population distribution of the anions departs from a purely statistical mixture (2:1), which would correspond to production from an infinitely hot source. The distribution can be used to estimate the temperature of the anions via the Boltzmann distribution, yielding a temperature of about 2400 ± 800 K, a value we consider reasonable. We have further measured the fine-structure populations for different ion source conditions, and found that the populations only weakly depend on the discharge current. This is expected since we are already in the asymptotic regime, where populations are close to statistical.

Finally, it is interesting to note that, although the branching ratios are not statistical, since the initial fine-structure distribution is close to statistical, so are the resulting population distributions of the final $O(^3P_{J'})$ and $O(^1D_{J'})$ levels. From the measured populations and theoretical branchings ratios, we obtain, e.g., 0.56 ± 0.03 for the $J' = 2$ component of the ground term, 0.33 ± 0.04 for its $J' = 1$ component, and 0.11 ± 0.04 for $J' = 0$. This is simply a result of the symmetry and orthogonality properties of the $6j$ symbols.

We are hence able to completely define the initial level of the anion and the final level of the atom, down to the fine-structure populations. These results are shown in Fig. 4 along with branching ratios calculated using Eq. (13). We are able to reach this level of detail both through velocity map imaging and also by examining the total cross section at threshold.

C. Asymmetry parameters

The measured asymmetry parameter for photodetachment of O^- leaving the oxygen atom in its ground term is shown in Fig. 8 and compared against available experimental and theoretical data. The present results follow the general trend established by Cooper and Zare [26], with isotropic emission

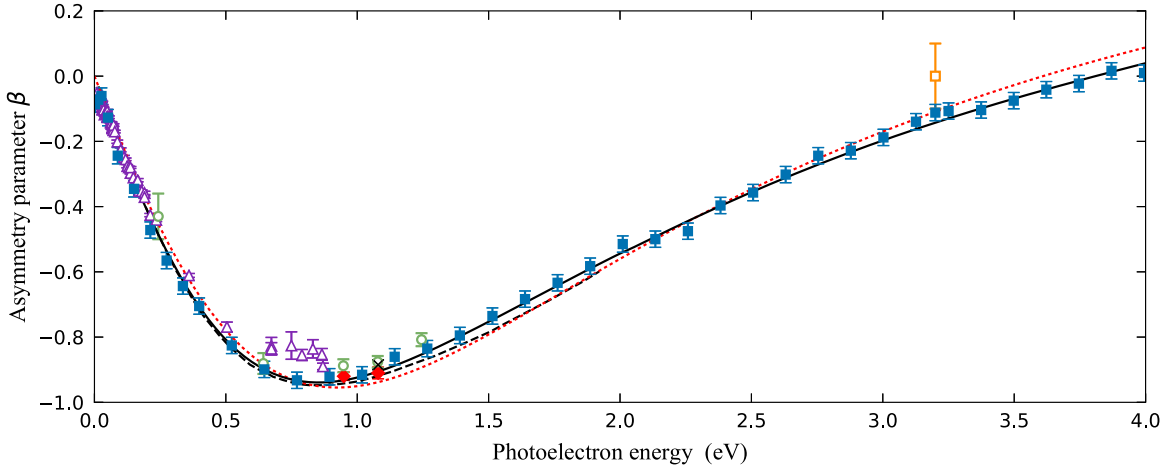

FIG. 8. Asymmetry parameter for photodetachment of O^- leaving O in the ^3P ground term. Full squares: present experiment; open triangles: Cavanagh *et al.* [31,32]; open circles: Hanstorp *et al.* [29]; full diamonds: Breyer *et al.* [28]; cross: Hall and Siegel [27]; open square: Domesle *et al.* [24]; dotted line: best fit to the present results using the model of Hanstorp *et al.* [29]; dashed line: Cooper and Zare [26]; full line: present R-matrix calculation in the length gauge.

at threshold ($\beta = 0$), emission preferentially perpendicular to the polarization axis ($\beta \simeq -1$) for intermediate photoelectron energies, and gradual return towards isotropic emission thereafter. This shape, characteristic of the photodetachment of electrons with $\ell \geqslant 1$, is the result of an interference between the competing s and d outgoing waves.

For photoelectron kinetic energies below 1.5 eV, the present data agree with all four existing measurements to within their error bars [27–29,31,32,57]. Hall and Siegel pioneered measurements of the photoelectron angular distribution by photodetaching a beam of O^- inside the cavity of an Ar^+ laser and collecting photoelectrons with a hemispherical energy analyzer of low solid angle acceptance [27]. By measuring the yield of photoelectrons while rotating the polarization of the laser light with a $\lambda/2$ plate, the angular distribution could be retrieved. A similar setup was later used by Breyer *et al.* [28]. Hanstorp *et al.* measured β by using an Ar^+ laser and a ring dye laser to photodetach O^- ions inside a graphite tube drilled with thin holes, outside of which a channel electron multiplier was used to collect photoelectrons [29]. Again, rotating the polarization of the laser light while recording the electron yield allows the angular distribution to be determined. Recently, Cavanagh *et al.* [31,32,57] measured the asymmetry parameter for photoelectron energies ranging from threshold to 1.2 eV using a high-resolution velocity map imaging spectrometer.

In the higher-energy region, the sole data available are the measurement of Domesle *et al.* at a wavelength of 266 nm (4.66 eV) [24]. They obtained β by measuring the photoelectron time of flight (TOF) inside a magnetic-bottle spectrometer and subsequently modeling trajectories with Monte Carlo methods. Their result (0.0 ± 0.1) is different from ours (-0.112 ± 0.035), but both agree within error bars. The reason for such a discrepancy is unclear. If we note that there is in fact good agreement for the $O(^1D)$ channel (see below), where the distribution is strongly asymmetrical ($\beta \simeq -1$), we may speculate that the fitting of the experimental electron TOF distribution with the Monte Carlo model is appropriate only for directional emission, and fails in the case of isotropic emission due to spurious nonisotropic effects.

The present experimental results are in fair agreement with those of Cooper and Zare [26], who established the eponymous formula for the asymmetry parameter and computed β using radial dipole matrix elements obtained from the model potential of Robinson and Geltman [12]. The Cooper and Zare formula has been further simplified by Hanstorp *et al.* [29], under the assumption that radial dipole matrix elements follow the Wigner threshold law:

$$\beta = 2A_2\varepsilon \frac{A_2\varepsilon - 2c}{1 + 2A_2^2\varepsilon^2}, \tag{15}$$

where ε is the photoelectron energy. The parameter A_2 is related to the ratio between the radial dipole matrix elements coupling the initial state and the s and d continua, and the parameter c is the cosine of the phase-shift difference between the s and d outgoing waves. We have fit our experimental data with the above formula, obtaining $A_2 = 0.535$ eV^{-1} and $c = 0.966$, compared with the values 1.1 eV^{-1} and 0.925 obtained by Hanstorp *et al.* for the fit of their results [29]. Agreement between the fit and the present values is satisfactory over a broad energy range, where most energies are already well beyond the range of validity of the Wigner threshold law used to derive Eq. (15). Such an extended agreement may be due to the fact that the Wigner law is used only to determine a ratio between two dipole matrix elements [29]. We further note that when restricting the present data to energies below 1.5 eV in the fitting procedure, the values of the parameters A_2 and c become similar to those of [29]. Furthermore, agreement between the fit and the present results is enhanced below 1.5 eV but degraded at higher photoelectron energies.

Our R-matrix results using polarized pseudostates are in very good agreement with the present measurement throughout the whole energy range. Only results in the length gauge are presented in Fig. 8 as those in the velocity gauge are indistinguishable on the scale of the figure. Close to threshold, the R-matrix results tend to be slightly larger than the measurements, while remaining just within the experimental error bars. The R-matrix results are also in good agreement with those obtained using the formula of Cooper and Zare up to about 1 eV, in particular for the position and depth of the minimum. At higher energies, the differences increase to about 5%. Finally, we note that the asymmetry parameter was also computed using density functional theory by Liu and Ning [19], however, the shape of their results greatly differs from that seen in Fig. 8.

Data concerning the asymmetry parameter for photodetachment leaving oxygen in its first excited term $O(^1D)$ are much scarcer. In Fig. 9, we present our current experimental results together with the only other measurement, by Domesle *et al.* [24] at a wavelength of 266 nm (4.66 eV). The agreement is very good. Also shown is the best fit of our results to the model of Hanstorp *et al.* [29] (with parameters $A_2 = 0.325$ eV^{-1} and $c = 0.925$), and the results from our R-matrix calculation using polarized pseudostates. The

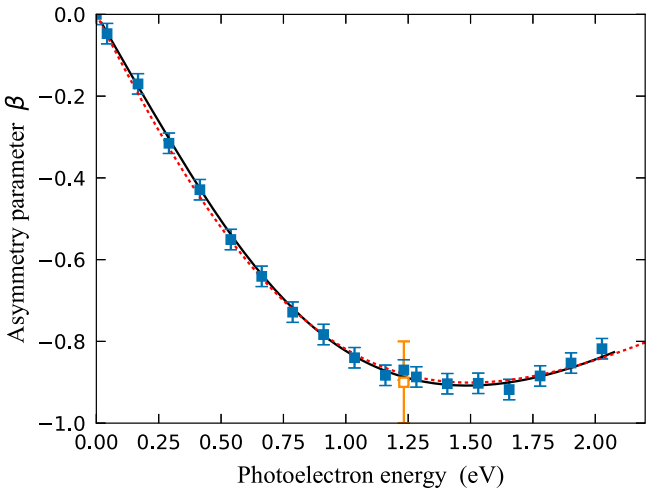

FIG. 9. Asymmetry parameter for photodetachment of O^- leaving O in the ^1D term. Full squares: present experiment; open square: Domesle *et al.* [24]; dotted line: best fit to the present results using the model of Hanstorp *et al.* [29]; full line: present R-matrix calculation in the length gauge.

agreement between our measured values and those of the R-matrix calculation is very good.

VI. CONCLUSION

We have reported on a joint experimental and theoretical study of the one-photon detachment of O^- for photon energies ranging from threshold (1.46 eV) to 5.5 eV, with the aim of presenting the most complete picture of the process in terms of total, partial, and differential cross sections. The absolute total cross section was measured using the animated-crossed-beam technique; the opening of the $O(^1D)$ reaction channel has been investigated in detail and absolute cross sections have been measured up to just below the $O(^1S)$ threshold. The new values are in good agreement with our previous study [9], and are about 15%–20% larger than those of earlier experiments, which have often been used to put measurements for other anions on an absolute scale. The results of the R-matrix calculations employing a small number of polarized pseudostates are in fairly good agreement with the new measurements; below the ^1D threshold the differences are of the order of 5%–10% while above this threshold the agreement is better than 5%. A VMI spectrometer designed for a fast anion beam was purpose-built in order to measure branching ratios, from which partial cross sections were obtained, as well as asymmetry parameters, related to differential cross sections. Branching ratios for the photodetachment of O^- are in fair agreement with the only other experimental value available [24], and, away from threshold, indicate that photodetachment leaves about 20% of the atoms in the $O(^1D)$ excited term while the rest are in the ground term. The partial cross sections extracted from the total cross section using the branching ratios are in good agreement with those obtained from the R-matrix calculation. The asymmetry parameters were measured for photon energies up to 5.5 eV, and for both final terms display the characteristic behavior of p-electron detachment, resulting in electron emission perpendicular to the laser polarization axis at intermediate photoelectron energies. There is good agreement with other available experimental data and with the results of our R-matrix calculation.

This study demonstrates that by combining well-established experimental techniques and widely tunable broadband laser systems, one can determine absolute values for the complete set of parameters governing photodetachment. The resulting data provide a wealth of information on the process and provide a stringent test for theoretical methods, for which photodetachment from open-shell anions is challenging. For example, calculations using the state-of-the-art B-spline R-matrix (BSR) approach [17], employing 108 target states and pseudostates with very accurate energies for more than 20 of the lowest bound states, but with less accurate values for the electron affinity and polarizability of the oxygen ground term, yielded total cross sections that are about 15% larger than our new measured values. In contrast, our current R-matrix calculation employs only three target states and six polarized pseudostates optimized on the polarizability of the oxygen ground term. While the values for the electron affinity and ground term polarizability are more accurate than those of the 108-state BSR calculation, and the cross sections agree much better with the experiment, the calculation is, however, limited in the range of photon energies that it can cover.

The experimental techniques employed are certainly not limited to O^- and can be applied to many other anions. Photodetachment of H^- is a widely used benchmark, and determining absolute cross sections over a larger range of photon energies is most certainly necessary. Photodetachment of C^- is of astrophysical importance for which reliable absolute cross sections are still lacking. Molecular anions can also be studied following the present procedure and the photodetachment of OH^- may be of particular interest. Finally, our approach is not limited to anions, and its application to neutral particles may be a perspective for future work.

ACKNOWLEDGMENTS

This work was supported by the Fonds de la Recherche Scientifique-FNRS under Grant No. 4.4504.10. Computational resources were provided by the Institut de Physique de Rennes.

[1] P. Defrance, F. Brouillard, W. Claeys, and G. V. Wassenhove, J. Phys. B: At. Mol. Phys. **14**, 103 (1981).
[2] F. Brouillard and P. Defrance, Phys. Scr. **T3**, 68 (1983).
[3] A. T. J. B. Eppink and D. H. Parker, Rev. Sci. Instrum. **68**, 3477 (1997).
[4] L. M. Branscomb, D. S. Burch, S. J. Smith, and S. Geltman, Phys. Rev. **111**, 504 (1958).
[5] S. J. Smith, *Proceedings of the 4th International Conference on Phenomena in Ionized Gases* (North-Holland, Amsterdam, Netherlands, 1959).
[6] L. M. Branscomb, S. J. Smith, and G. Tisone, J. Chem. Phys. **43**, 2906 (1965).
[7] L. C. Lee and G. P. Smith, J. Chem. Phys. **70**, 1727 (1979).
[8] P. Hlavenka, R. Otto, S. Trippel, J. Mikosch, M. Weidemüller, and R. Wester, J. Chem. Phys. **130**, 061105 (2009).
[9] M. Génévriez, X. Urbain, A. Dochain, A. Cyr, K. M. Dunseath, and M. Terao-Dunseath, Phys. Rev. A **94**, 023407 (2016).
[10] R. J. W. Henry, Phys. Rev. **162**, 56 (1967).
[11] J. W. Cooper and J. B. Martin, Phys. Rev. **126**, 1482 (1962).
[12] E. J. Robinson and S. Geltman, Phys. Rev. **153**, 4 (1967).
[13] W. R. Garrett and H. T. Jackson, Phys. Rev. **153**, 28 (1967).
[14] V. K. Lan, N. Feautrier, M. L. Dourneuf, and H. V. Regemorter, J. Phys. B: At. Mol. Phys. **5**, 1506 (1972).
[15] R. M. Stehman and S. B. Woo, Phys. Rev. A **20**, 281 (1979).
[16] W. Jian-Hua, Y. Jian-Min, and V. K. Lan, Chin. Phys. **12**, 1390 (2003).
[17] O. Zatsarinny and K. Bartschat, Phys. Rev. A **73**, 022714 (2006).
[18] C. M. Oana and A. I. Krylov, J. Chem. Phys. **131**, 124114 (2009).

[19] Y. Liu and C. Ning, J. Chem. Phys. **143**, 144310 (2015).
[20] M. L. Seman and L. M. Branscomb, Phys. Rev. **125**, 1602 (1962).
[21] G. Haeffler, D. Hanstorp, I. Y. Kiyan, U. Ljungblad, H. H. Andersen, and T. Andersen, J. Phys. B: At. Mol. Opt. Phys. **29**, 3017 (1996).
[22] P. Kristensen, H. H. Andersen, P. Balling, L. D. Steele, and T. Andersen, Phys. Rev. A **52**, 2847 (1995).
[23] D. S. Burch, S. J. Smith, and L. M. Branscomb, Phys. Rev. **112**, 171 (1958).
[24] C. Domesle, B. Jordon-Thaden, L. Lammich, M. Förstel, U. Hergenhahn, A. Wolf, and H. B. Pedersen, Phys. Rev. A **82**, 033402 (2010).
[25] R. L. Chase and H. P. Kelly, Phys. Rev. A **6**, 2150 (1972).
[26] J. Cooper and R. N. Zare, J. Chem. Phys. **48**, 942 (1968).
[27] J. L. Hall and M. W. Siegel, J. Chem. Phys. **48**, 943 (1968).
[28] F. Breyer, P. Frey, and H. Hotop, Z. Phys. A **286**, 133 (1978).
[29] D. Hanstorp, C. Bengtsson, and D. J. Larson, Phys. Rev. A **40**, 670 (1989).
[30] M. Génévriez and X. Urbain, Phys. Rev. A **91**, 033403 (2015).
[31] S. J. Cavanagh, S. T. Gibson, M. N. Gale, C. J. Dedman, E. H. Roberts, and B. R. Lewis, Phys. Rev. A **76**, 052708 (2007).
[32] S. J. Cavanagh, S. T. Gibson, and B. R. Lewis, J. Phys.: Conf. Ser. **212**, 012034 (2010).
[33] I. León, Z. Yang, H.-T. Liu, and L.-S. Wang, Rev. Sci. Instrum. **85**, 083106 (2014).
[34] C. J. Johnson, B. B. Shen, B. L. J. Poad, and R. E. Continetti, Rev. Sci. Instrum. **82**, 105105 (2011).
[35] B. F. Parsons, S. M. Sheehan, K. E. Kautzman, T. A. Yen, and D. M. Neumark, J. Chem. Phys. **125**, 244301 (2006).
[36] X. Urbain, D. Bech, J.-P. Van Roy, M. Géléoc, S. J. Weber, A. Huetz, and Y. J. Picard, Rev. Sci. Instrum. **86**, 023305 (2015).
[37] B. Dick, Phys. Chem. Chem. Phys. **16**, 570 (2014).
[38] UK APAP (Atomic Processes for Astrophysical Plasmas network), http://www.apap-network.org/.
[39] P. G. Burke, *R-Matrix Theory of Atomic Collisions*, Springer Series on Atomic, Optical, and Plasma Physics, Vol. 61 (Springer, Berlin, 2011).
[40] E. Clementi and C. Roetti, At. Data Nucl. Data Tables **14**, 177 (1974).
[41] A. Hibbert, Comput. Phys. Commun. **9**, 141 (1975).
[42] V. K. Lan, M. Le Dourneuf, and P. G. Burke, J. Phys. B: At. Mol. Phys. **9**, 1065 (1976).
[43] R. Alpher and D. White, Phys. Fluids **2**, 153 (1959).
[44] K. Andersson and A. J. Sadlej, Phys. Rev. A **46**, 2356 (1992).
[45] M. Medveď, P. W. Fowler, and J. M. Hutson, Mol. Phys. **98**, 453 (2000).
[46] C. Blondel, C. Delsart, C. Valli, S. Yiou, M. R. Godefroid, and S. Van Eck, Phys. Rev. A **64**, 052504 (2001).
[47] NIST Atomic Spectra Database, http://www.nist.gov/pml/data/asd.cfm.
[48] D. Marinov, J.-P. Booth, C. Drag, and C. Blondel, J. Phys. B **50**, 065003 (2017).
[49] D. M. Neumark, K. R. Lykke, T. Andersen, and W. C. Lineberger, Phys. Rev. A **32**, 1890 (1985).
[50] T. Suzuki and T. Kasuya, Phys. Rev. A **36**, 2129 (1987).
[51] C. Blondel, W. Chaibi, C. Delsart, C. Drag, F. Goldfarb, and S. Kröger, Eur. J. Phys. D **33**, 335 (2005).
[52] G. Miecznik and C. H. Greene, Phys. Rev. A **53**, 3247 (1996).
[53] E. P. Wigner, Phys. Rev. **73**, 1002 (1948).
[54] A. R. P. Rau and U. Fano, Phys. Rev. A **4**, 1751 (1971).
[55] C. Pan and A. F. Starace, Phys. Rev. A **47**, 295 (1993).
[56] W. C. Lineberger and B. W. Woodward, Phys. Rev. Lett. **25**, 424 (1970).
[57] S. J. Cavanagh, S. T. Gibson, and B. R. Lewis, J. Phys.: Conf. Ser. **194**, 022026 (2009).